HHS Public Access

Author manuscript

IEEE Access. Author manuscript; available in PMC 2024 October 17.

Published in final edited form as:

IEEE Access. 2024 ; 12: 45369–45380. doi:10.1109/access.2024.3377664.

Optimal Wavelet Selection for Signal Denoising

GYANA RANJAN SAHOO[1], **JACK H. FREED**[1,2], **MADHUR SRIVASTAVA**[1,2,3] **[Member, IEEE]**

[1]Department of Chemistry and Chemical Biology, Cornell University, Ithaca, NY 14853, USA

[2]National Biomedical Center for Advanced ESR Technology, Cornell University, Ithaca, NY 14853, USA

[3]Cornell Atkinson Center for Sustainability, Cornell University, Ithaca, NY 14853, USA

Abstract

Wavelet denoising plays a key role in removing noise from signals and is widely used in many applications. In denoising, selection of the mother wavelet is desirable for maximizing the separation of noise and signal coefficients in the wavelet domain for effective noise thresholding. At present, wavelet selection is carried out in a heuristic manner or using a trial-and-error that is time consuming and prone to error, including human bias. This paper introduces a universal method to select optimal wavelets based on the sparsity of Detail components in the wavelet domain, an empirical approach. A mean of sparsity change (μ_{sc}) parameter is defined that captures the mean variation of noisy Detail components. The efficacy of the presented method is tested on simulated and experimental signals from Electron Spin Resonance spectroscopy at various SNRs. The results reveal that the μ_{sc} values of signal vary abruptly between wavelets, whereas for noise it displays similar values for all wavelets. For low Signal-to-Noise Ratio (SNR) data, the change in μ_{sc} between highest and second highest value is ≈ 8 – 10% and for high SNR data it is around 5%. The mean of sparsity change increases with the SNR of the signal, which implies that multiple wavelets can be used for denoising a signal, whereas, the signal with low SNR can only be efficiently denoised with a few wavelets. Either a single wavelet or a collection of optimal wavelets (i.e., top five wavelets) should be selected from the highest μ_{sc} values. The code is available on GitHub and the signalsciencelab.com website.

Keywords

Wavelet selection; decomposition level selection; detail components; signal denoising; sparsity; wavelet denoising; wavelet transform

Corresponding author: Madhur Srivastava (ms2736@cornell.edu).

CODE AVAILABILITY

Matlab code written for this work can be found in public GitHub repository (https://github.com/Signal-Science-Lab/Optimal-wavelet-selection-for-signal-denoising) and Signal Science Lab website (www.signalsciencelab.com).

I. INTRODUCTION

Often, experimental signals are weak and are difficult to study due to the presence of noise. Wavelet denosing is widely used to improve the Signal-to-Noise Ratio (SNR) without distorting the signal [1], [2], [3], [4], [5], [6]. Wavelet denoising is known to have better performance over filtering based denoising methods [3], [4] and has been applied to many fields such as time series analysis [5], [6], [7], computed tomography [8], [9], [10], magnetic resonance imaging [11], [12], [13], fluorescence imaging [14], [15], [16], Raman spectroscopy [17], [18], [19], speech recognition [20], [21], [22], traffic volume prediction [23], [24], [25] and electron spin resonance (ESR) spectroscopy [1], [26], [27].

The efficacy of denoising depends on several factors like selection of the mother wavelet, decomposition level and thresholding criteria [28], [29], [30]. Currently, noise thresholding and decomposition level selection for discrete wavelet transforms are well developed. However, the mother wavelet for effective denoising has been selected heuristically and/or through trial and error. The mother wavelet plays a crucial role in denoising and hence needs to be selected carefully. Sub-optimal wavelet selection can lead to signal distortion or inadequate noise reduction.

A mother wavelet that maximizes the magnitude of the signal coefficient and minimizes the noise coefficient values in the wavelet domain would yield better efficacy in denoising. Several methods have previously been developed for optimal wavelet selection using cross validation [31], Shannon entropy [32], cross correlation and signal-to-noise-ratio [33], [34], [35], degree of energy variation [36], probabilistic neural network [37] and Nash Sutcliffe criteria [38]. However, these methods are not universal and focus only on specific types of signal [31], [32], [37], [38], [39]. Also, the wavelet and decomposition level selections are not performed in the wavelet domain. Instead, they are obtained after comparing the denoised data, which makes the method cumbersome, time consuming and difficult to apply in real time.

In this paper, a generalized method is presented to select the optimal mother wavelet function for denoising. The method uses a sparsity parameter [1], [40] to quantify maximum separation between signal and noisy Detail coefficients of the wavelet-transformed data. Subsequently, it calculates the mean of sparsity change to identify a wavelet (or a group of wavelets) that yields maximum separation across decomposition levels. The sparsity change has been reliably used to obtain the highest decomposition level [40], and hence can be easily integrated into any wavelet denoising algorithm. Using this sparsity criterion, an automated empirical method is developed that selects the optimal wavelet in real time for a given noisy signal, without a *priori* knowledge.

The paper is organized as follows. In section II, we discuss the importance of wavelet families and respective wavelets used for this study. In section III, we provide the details of effective decomposition level selection, sparsity calculation and its use to select a decomposition level that separates noisy and noise-free Detail components. In section IV, we describe criteria used to select the optimal wavelets. In section V, we explain the model data, including simulated and experimental data, which is used to test and validate our method.

Section VI, discusses the results and Section VII summarizes the method and findings in the Conclusion.

II. WAVELET SAMPLE SPACE

We created a sample space of most widely utilized wavelets for denoising. These include Biorthogonal, Coiflet, Daubechies, Reverse biorthogonal and Symlet families. Within each wavelet family we used bior1.1-bior2.6, coif1-coif5, db2-db11, rbio1.3-rbio2.8 and sym2-sym7, which have different filter lengths and practical applications. We did not consider db1 and rbio1.1, as they are the same as bior1.1 and haar, but with different names. Figure 1 displays mother wavelet families and their respective low and high pass filter coefficients. Table 2 displays the list of wavelets used in the sample space. It is worth mentioning that other and/or new wavelets can be added to the wavelet sample space.

III. DECOMPOSITION LEVEL SELECTION

A. EFFECTIVE DECOMPOSITION LEVEL

The maximum possible wavelet decomposition level ($= log2(length(X))$, where X is the input signal) for any signal is decided by its $length$. Yet, not all of them contain noise or signal. The signal coefficients after a certain decomposition level saturates, which suggests that the wavelet filter dominates the Detail components instead of the signal or noise coefficients. Thus, it can be calculated by taking the ratio of the length of Detail component and the length of the wavelet filter as given by;

$$R_j = \frac{L_{D_j}}{L_f} \tag{1}$$

where L_{D_j} is the length of Detail component at the jth decomposition level and L_f is the length of the wavelet filter. The maximum possible decomposition level is obtained when $R_j > 1.5$ [40]. For instance, Table 3 shows R_j associated with L_{D_j} and L_f for different wavelets in the Coiflet family at a given signal length of 1024. It can be seen that L_{D_j} values are different for each wavelet which is also reflected in R_j. The R_j reflects the dominance of the wavelet filter in a Detail component. Table 4 exhibits the effective decomposition level and corresponding ratio cutoff (> 1.5) for each wavelet in the wavelet sample space. It can be seen from Table 4, that the effective decomposition level varies for different wavelets based on their filter length.

B. SPARSITY

Sparsity captures the presence of noise in a Detail component, enabling the separation of noisy and noise-free Detail components. The Detail components with larger noise has lower sparsity values, whereas $D_j's$ with lower noise has larger sparsity [1], [40]. The presence of noise in Detail coefficient decreases with increase in decomposition level, which results in increase in sparsity. Sparsity (S) of Detail coefficients (D) at each level for all wavelets is calculated as per the following equation.

$$S_j = \frac{max|D_j|}{\sum_{k=1}^{q_j} |D_j[k]|}, \quad 1 \le j \le N \tag{2}$$

where S_j, D_j and q_j are the sparsity, Detail component and length of the Detail component at j^{th} decomposition level, respectively. Figure 2a and 2b displays the sparsity plot of sym2 and coif2 wavelets, of white Gaussian noise, noise-free and noisy signal at SNR-30, respectively. It can be seen that, at a lower decomposition level, the sparsity value of the noisy signal is close to that of the sparsity value of only noise, whereas the sparsity value of the noisy signal is close to the sparsity value of noise-free data at higher decomposition levels. This separation between noisy and noise-free Detail components is highlighted by a vertical line in all the sparsity plots shown in Figure 2. This feature is consistent across other simulated signals, which can be seen in the sparsity plot of SNR-10 data shown in Figure 2c and 2d for sym2 and coif2 wavelets respectively.

C. SPARSITY CHANGE (ΔS)

The sparsity change parameter is used to determine the highest decomposition level that contains a noisy Detail component. Sparsity value represents the magnitude of noise present in a Detail component, whereas, the sparsity change separates noisy and noise-free Detail components by identifying an abrupt change in ΔS value between adjacent decomposition levels. The sparsity change (ΔS) is calculated as

$$\Delta S_j = S_j - S_{j-1} \tag{3}$$

where ΔS_j is the sparsity change at jth decomposition level and S_j, and S_{j-1} are the sparsity at jth and $(j-1)th$ decomposition level respectively. $\Delta S_1 = 0$ as there is no preceding level.

D. OPTIMAL DECOMPOSITION LEVEL (κ)

The optimal decomposition level (κ) that separates noisy and noise free Detail components can be calculated subjectively from change in sparsity plot or empirically through a cutoff value [40]. In the subjective approach, the optimal decomposition level j (= κ) is selected where the first abrupt change in the ΔS_j plot happens between j and j + 1. Empirically, a threshold of 5% with respect to 1 is selected as cutoff between noisy and noise-free Detail components. The optimal decomposition level (κ =) j − 1 is selected where $\Delta S_j > 0.05$ in the first occurrence [40].

IV. WAVELET SELECTION

Selection of wavelets is done using the sparsity of the Detail coefficients. The mean of ΔS between adjacent levels is used as the quantitative parameter to select optimal wavelet.

A. MEAN OF SPARSITY CHANGE (μ_{SC})

The mean of ΔS for each wavelet is calculated between level-2 to one level after the optimal decomposition level $(\kappa + 1)$. $\Delta S_1 = 0$ as there is no preceding level. Hence, the mean of ΔS for each wavelet is calculated between levels 2 to $\kappa + 1$ using equation 4. Now, μ_{sc} can be expressed as the ratio of difference in sparsity between level $\kappa + 1$ and level 1 to $(\kappa - 1)$. The plot of μ_{sc} of white Gaussian noise, noise-free signal and noisy signal of SNR-30 displayed in Figure 3 demonstrates the variation of μ_{sc} among wavelets. From the Figure 3, it can be seen that the μ_{sc} of noise is lower, whereas, μ_{sc} for noise-free signal and noisy signal are comparable. Such behavior demonstrates the efficacy of the method to reduce effect of noise while selecting optimal wavelet. It should be noted that the mean of sparsity for noise is calculated between the decomposition level 2 and optimal decomposition level obtained corresponding to the noisy signal.

$$\begin{aligned}\mu_{sc} &= \frac{\sum_{j=2}^{\kappa+1} \Delta S_j}{(\kappa+1)-2} \\ &= \frac{\Delta S_2 + \Delta S_3 + \ldots + \Delta S_{\kappa+1}}{\kappa - 1} \\ &= \frac{(S_2 - S_1) + (S_3 - S_2) + \ldots + (S_{\kappa+1} - S_\kappa)}{\kappa - 1} \\ &= \frac{S_{\kappa+1} - S_1}{\kappa - 1}\end{aligned} \tag{4}$$

B. WAVELET SELECTION CRITERIA

Optimal wavelets are selected utilizing the mean of sparsity change. From Figure 3, it can be seen that μ_{sc} of only noise has similar values for all wavelets. On the other hand, μ_{sc} of noise-free signal for bior2.2 wavelet has higher value compared to other wavelets. For a noisy signal few wavelets have higher μ_{sc} value than others. Such behavior demonstrates that, there can be only one or two optimal wavelets for high SNR signal whereas for low SNR signal there can be a few optimal wavelets. The wavelet corresponding to the highest μ_{sc} is selected as the optimal wavelet. Additionally, we have selected five wavelets corresponding to highest μ_{sc} values. Mathematically, the optimal wavelet and five optimal wavelets can be selected as

$$\begin{aligned}\text{Optimal wavelet} &= wavelet\left\{max\left(\mu_{sc}^1, \mu_{sc}^2, \cdots, \mu_{sc}^n\right)\right\} \\ \text{Five optimal wavelets} &= \sum_{i=1}^{5} wavelet\left\{max\left(\mu_{sc}^1, \mu_{sc}^2, \cdots, \mu_{sc}^{n+1-i}\right)\right\}\end{aligned} \tag{5}$$

where *wavelet* is the list of wavelets in the sample space, n is the total number of wavelets, μ_{sc}^n is the mean of sparsity corresponding to n^{th} wavelet.

V. DATA COLLECTION

A. SIMULATED DATA

Simulated ESR data is obtained using the Lorentz function written in MATLAB. The data generated has length of 1024 having identical peaks of height approximately 0.2753 with separation between the peaks of around 185 index values and the space between positive and negative peaks is 13 index values. The amplitude of the signals are symmetric and oscillates between positive and negative values with zero mean. Noise-free (red line) and noisy (blue line) simulated signal of SNR-10 are displayed in Figure 4. To generate signals of various SNRs, additive white Gaussian noise is added to the signal. Signals of SNRs 5, 10, 30, and 50 are generated through this method and the SNR is calculated utilizing the formula given in equation 6. $\text{Noise}_{\text{rms}}$ is calculated from the first 200 index values of the input signal and the region is highlighted inside the rectangle in Figure 4.

$$SNR = \frac{Signal_{peak}}{Noise_{rms}} \tag{6}$$

B. EXPERIMENTAL DATA COLLECTION

The results obtained from simulated data are tested on an experimental signal recorded through continuous wave-Electron Spin Resonance (cw-ESR) spectroscopy experiments. CW-ESR is used extensively to study unpaired electrons to understand the dynamics and structure of biomolecules, and is the most commonly used ESR technique [41]. The cw-ESR spectrum is acquired in the magnetic field (B_0) domain, which is linearly swept, i.e. $B_0 = B_0(t)$, increasing in magnetic field over time. The samples are irradiated continuously with microwave frequency radiation till a resonance condition is achieved, where the energy supplied by the microwave radiation is sufficient for the unpaired electron to switch its spin state from aligned to anti-parallel, generating the signal at the detector. In cw-ESR, a number of parameters are optimized simultaneously, to increase SNR without distorting the signal. Magnetic field sweep time, the time constant/ spectrometer response time (which filters out noise, at the risk of broadening or filtering out the signal), and the number of scans are few such parameters. An additional oscillating magnetic field is superimposed which oscillates with a ΔB of a few Gauss at 100kHz. This ‘modulation frequency’ is responsible for improving the SNR by ensuring phase-sensitive detection, where only the 100kHz oscillations are captured by the lock-in amplifier. Depending on the applied amplitude of this modulating field, a range of signals are detected in the spectrum, and resulting in a first derivative mode spectrum. If the modulation amplitude is too high relative to the signal linewidth, it will broaden the signal. The microwave power is adjusted such that the signal is generated without saturating the signal, which also causes broadening effects. Also present in cw-ESR is a baseline signal, which varies depending on the spectrometer and resonator used, and in the case of nitroxide spectra, it represents a small fraction of the signal measured.

The ESR experiments were carried out at 20°C using a commercial spectrometer (BRUKER ELEXYS-II E500) operated at a microwave frequency of 9.4 GHz corresponding to a static magnetic field of 0.34 Tesla. The sample consists of 4 μL of a 100 μM aqueous solution of the commonly used spin-probe molecule Tempol (4-Hydroxy-2,2,6,6-Tetramethylpiperdine 1-oxyl) [41], [42], [43], [44], which helps form a stable but ESR-active adduct. The magnetic field was then swept over a range of 60 G corresponding to the resonant spectral range which took 2 minutes, and a 82 ms time constant was used. The spectral data consisted of 4096 points along the magnetic field sweep. In addition, small coils placed at the sides of the resonator provided a small magnetic field modulation of ±0.02 G at a frequency of 100 kHz. The first derivative of absorption signal was recorded using a lock-in detector locked at 100 kHz frequency [41]. Low power (0.2 mW) microwave radiation was used to avoid saturating the ESR signal. Multi-scan experiments were performed with a delay of 4 s between scans. The results of these scans were then averaged. For reference, ESR data collected from the spectrometer averaged at 500 scans is shown in Figure 5a. The characteristic three-line spectrum arises from the interaction between the electrons and the nitrogen-14 nucleus of the nitroxide sample.

In another set of experiments, an ESR signal was acquired from a sample prepared in a different environment to obtain a complex spectrum. It was obtained on a home-built (ACERT) 95 GHz ESR spectrometer [44] with a DC magnetic field of 3.3 Tesla at 25°C. The sample here contained ca. 5 μL of phospholipid vesicles doped with 0.5% of a lipid spin label: 16–PC (1-acyl-2-[16-(4,4-dimethyloxazolidine-N-oxyl)stearoyl]-sn-glycero-3-phosphocholine) in the fluid phase that has been suspended in water. It was placed in a disc-like sample holder utilized for millimeter-wave ESR methodology [44]. This nitroxide sample contains the same three-line spectrum, however it has it's motion restricted in the lipid vesicle, revealing the orientation dependence of the spectrum, and this is further resolved by measuring at a high magnetic field. The acquisition parameters were: sweep width of 250 G, sweep time of 2 minutes with a time constant of 100 ms. The millimeter-wave power was 16 mW and the spectrum consists of 512 points. The field modulation parameters were: 6 G modulation amplitude and 100 kHz modulation frequency. The time between scans was 3 seconds. Reference ESR signal recorded from the in-house built spectrometer is displayed in Figure 5b.

VI. RESULTS AND DISCUSSION

A. SIGNAL WITH VARIABLE NOISE

Sparsity, sparsity change and mean of sparsity change are used for optimal wavelet selection. μ_{sc} is used as a quantitative parameter to select the optimal wavelets. The method is first tested on simulated signals with variable SNR of 5, 10, 30 and 50. Figure 6a and 6b displays the white Gaussian noise generated to achieve signal SNR of 5 and 30 respectively. The difference in noise level is clearly visible in Figure 6c and 6d which exhibits the simulated signal of SNR 5 and 30 respectively. The sparsity plot of simulated white Gaussian noise (generated to achieve SNR-5), noise-free signal and noisy signal of SNR-5 for bior1.1 is shown in Figure 6e. Bior1.1 is obtained as the optimal wavelet that maximizes the difference between noisy and noise-free Detail components for the simulated signal of SNR-5. It can

be seen from the sparsity plot in Figure 6e that the sparsity values of noise-free and noisy signals are converging at a higher decomposition level, which demonstrates that the noise in the signal is represented by the first few Detail components and the signal by the next few Detail components. Also the sparsity values at decomposition level 8 are similar for all three cases, which demonstrates that, at higher decomposition level the filters dominate the Detail components instead of the signal. The optimal decomposition level for wavelet bior1.1, when applied to the signal of SNR-5 is found to be 3, which is indicated by a vertical line between level 3 and 4 in Figure 6e. The sparsity values for noise and a noisy signal at decomposition level 3 are similar, whereas the sparsity value at level 4 for a noisy signal is higher and is also close to the sparsity value of a noise-free signal. This demonstrates the optimal decomposition level obtained for the selected wavelet maximizes separation between noisy and noise-free Detail components. For a signal of SNR-30 the optimal wavelet from our method is found to be bior2.6. The optimal decomposition level obtained using the bior2.6 wavelet for a signal of SNR-30 is 2. Again similar behavior is observed in the case of signal of SNR-30 and wavelet bior2.6 as illustrated previously. From Figure 6f, it can be seen that, the sparsity values after optimal decomposition level ($\kappa = 2$) are closer to the sparsity value of a noise-free signal and are similar ti the sparsity value of noise before level-2. This reiterates the fact that the optimal decomposition level for the selected wavelet effectively distinguishes noisy and noise-free Detail components. It should be noted that a similar trend in sparsity is observed for all other simulated and experimental signals.

The mean of sparsity change of noise-free signal shown in Figure 3 displays abrupt variation for different wavelets. However, the μ_{sc} of only noise have similar values. Such behavior demonstrates that the analysis with few wavelets perform better in separating noise and signal in the wavelet domain. The stem plot of the μ_{sc} of all the wavelets for simulated data of SNR-5, 10 and 30 shown in the Figure 6g manifests an overall increase in the μ_{sc} value with increase in SNR of the data. The increase in the μ_{sc} value for higher SNR data can be be attributed to the decrease in κ, that separates noisy and noise-free Detail coefficients. The mean of ΔS calculated across levels averages out the sparsity of noisy and noise-free Detail components between decomposition levels. This can be confirmed from Table 5, which demonstrates the decrease in κ of wavelets with an increase in SNR of the data, barring a few outliers. Wavelets with the highest μ_{sc} values are chosen as the optimal wavelets because it magnifies the separation between noisy and noise-free Detail components at a lower decomposition level. Consequently, noise-free components will represent the maximum signal and have the minimal effect of the filter function. Here, we have selected five wavelets corresponding to the highest μ_{sc} as our optimal wavelets. Table 5 displays the selected wavelets based on the highest μ_{sc} values and corresponding decomposition level and the μ_{sc} values.

B. EXPERIMENTAL DATA

The method developed for wavelet selection is validated on averaged ESR signals at different scans recorded through commercial and in-house built spectrometers. Signals of varying SNR collected from the commercial spectrometer are averaged at 1 scan, 4 scans

and 500 scans and in-house built spectrometer averaged at 1 scan, 4 scans and 18 scans are shown in Figure 5a and 5b respectively. It can be seen from the Figure that the SNR of the signal increases when averaged at higher scans. μ_{sc} plots of all three signals recorded from the commercial spectrometer shown in Figure 7c exhibits an increase in μ_{sc} with the signal averaged at higher scans. Figure 7d displays the stem plot of μ_{sc} for signals averaged at 1 scan, 4 scans and 18 scans collected using the in-house built spectrometer. The trends for μ_{sc} seen in the simulated data are also visible here. Similar to simulated data, this increase in μ_{sc} can be attributed to the increase in SNR of the averaged signal.

The optimal wavelets, corresponding κ and normalized μ_{sc} obtained from each experimental signal are shown in Table 6 and 7 for data collected from the commercial and in-house built spectrometer, respectively. Again, the higher μ_{sc} values for high SNR signal can be due to the averaging over too few levels.

VII. CONCLUSION

In this work, we present a sparsity based method for the optimal wavelet selection of noisy data. The algorithm uses the mean of sparsity change (μ_{sc}) as a quantitative parameter and facilitates the selection of optimal wavelets for effective denoising. The following conclusions are drawn from this work:

- The mean of sparsity change of noise has similar values for all wavelets, whereas the μ_{sc} for signal displays a larger value for one wavelet compared to others in the wavelet sample space.
- The mean of sparsity change increases with increase in SNR of the signal which can be attributed to the decrease in optimal decomposition level that separates noisy and noise-free Detail components.
- For low SNR signal, Biorthogonal wavelets perform better in separating noise and signal in the wavelet domain.

The technique presented here is advantageous over time consuming standard trial-and-error practice of wavelet selection. We have tested the method on simulated data and validated over experimental signals. The technique can be integrated to any wavelet based algorithms as a preprocessing tool for the selection of wavelets.

ACKNOWLEDGMENT

The authors would like to thank Dr. Tufa Assafa for the fruitful discussions and inputs to improve the manuscript. They would like to thank the National Biomedical Resource for Advanced Electron Spin Resonance Spectroscopy (ACERT) for providing the experimental data.

This work was supported by the National Institute of General Medical Sciences/National Institutes of Health under Grant R24GM146107, Grant R35GM151218, and Grant R35GM148272.

Biographies

GYANA RANJAN SAHOO received the B.Sc. degree from the S. V. M. College, Utkal University, Bhubaneswar, India, in 2011, the M.Sc. degree from the Department of Physics, Utkal University, in 2013, and the Ph.D. degree in physics from the Indian Institute of Technology Kanpur, India, in 2020.

From 2020 to 2021, he was a Research Assistant with the Department of Physics, Indian Institute of Technology Kanpur. Since 2021, he has been a Postdoctoral Research Associate with the Department of Chemistry and Chemical Biology, Cornell University, Ithaca, NY, USA. His research interests include signal processing, wavelet analysis, image segmentation, machine learning, optical spectroscopy, and imaging diagnostics.

JACK H. FREED received the B.E. degree in chemical engineering from Yale University, New Haven, CT, USA, in 1958, and the M.S. and Ph.D. degrees in chemistry from Columbia University, New York, NY, USA, in 1959 and 1962, respectively.

He was a Postdoctoral Fellow with the University of Cambridge, Cambridge, U.K., from 1962 to 1963. In 1963, he was a Faculty Member with Cornell University, Ithaca, NY, USA, where he has spent his subsequent career as an Assistant Professor (1963–1967), an Associate Professor (1967–1973); a Professor (1973–2016), an Emeritus (since 2016); and a Frank and Robert Laughlin Professor of physical chemistry (since 2007). He has been the Director of the National Biomedical Center for Advanced ESR Technology, since 2001. He has also held positions as a Visiting Scientist with the U.S. Japan Cooperative Science Program, Tokyo University, Japan, in 1969; a Guest Professor with Aarhus University, Denmark, in 1974; a Visiting Professor with the University of Geneva, Switzerland, in 1977, the Delft University of Technology, The Netherlands, in 1978, École Normale Supérieure, Paris, France, from 1984 to 1985, and the University of Padua, Italy, in 1991; a Charles A. MacDowell Lecturer of chemical physics with The University of British Columbia, in 1997; a Distinguished Visiting Professor with Yamagata University, Japan, in 1998; a Visiting Scientist with the University of Oxford, U.K., from 2007 to 2013; and a Israel Pollak Distinguished Lecturer with Technion, Israel, in 2009. He has authored over 400 publications and holds several patents. His research interests include the development of modern technology for electron-spin resonance (ESR) spectroscopy both in the development of modern spectrometers and in the theoretical interpretation of

ESR experiments designed to elucidate the structural dynamics of complex fluids, such as liquid crystals and membranes and the structure/function of membrane proteins and protein complexes.

Prof. Freed is a fellow of the American Physical Society, in 1976; the American Academy of Arts and Sciences, in 1994; the Royal Society of Chemistry, in 2009; and the American Association for the Advancement of Science, in 2009. He has also been an Honorary U.S. Ramsay Memorial Fellow (1962–1963); an NSF Postdoctoral Fellow with Cambridge University (1962–1963); an A. P. Sloan Foundation Fellow (1966–1968); the Weizmann Institute of Science Senior Fellow (1970); the John Simon Guggenheim Memorial Fellow (1984–1985) with the Institute for Advanced Studies, The Hebrew University of Jerusalem (1990); and an Inaugural Fellow of the International Society of Magnetic Resonance (2008). In 2001, he became an Honorary Member of the National Magnetic Resonance Society of India. Since 2006, he has been on the External Advisory Board of the National High Magnetic Field Laboratory, USA. He received the BuckWhitney Award in Pure and Applied Chemistry by the American Chemical Society (ACS), in 1981; the Bruker Award in ESR by the Royal Society of Chemistry, in 1990; the International Electron Spin Resonance Society Gold Medal, in 1994; the Irving Langmuir Prize in Chemical Physics by the American Physical Society, in 1997; the Zavoisky Prize in ESR by the Russian Academy of Sciences, in 1998; the E. Bright Wilson Award in Spectroscopy by ACS, in 2008; the ISMAR Prize from the International Society of Magnetic Resonance, in 2013; and the Joel H. Hildebrand Award in the Chemistry of Liquids by the ACS, in 2014. In honor of his extensive achievements, the *Journal of Physical Chemistry* issued a special J. H. Freed Festschrift Issue in 2004 on his 65th birthday. He has chaired the Gordon Research Conference on Magnetic Resonance in 1975. From 2008 to 2010, he was the President of the International EPR/ESR Society. He has served on many journal editorial boards, including *The Journal of Chemical Physics* (1976–1978), *The Journal of Physical Chemistry* (1979–1983), *Chemical Physics Letters* (1988–1990), *Applied Magnetic Resonance* (1990–2016), and *Magnetic Resonance Review* (1994–2000); and was an Associate Editor of the *Journal of Magnetic Resonance* (2007–2010).

MADHUR SRIVASTAVA (Member, IEEE) received the B.Tech. degree in electronics and communication engineering from the Jaypee University of Engineering and Technology (JUET), Guna, India, in 2011, and the M.Eng. degree in electrical and computer engineering and the M.S. and Ph.D. degrees in biomedical engineering from Cornell University, Ithaca, NY, USA, in 2012, 2016, and 2018, respectively.

In 2019, he accepted a faculty member position with the Department of Chemistry and Chemical Biology, Cornell University, where he is currently an Assistant Research Professor. He has been a Visiting Scholar with the Medical Research and Clinical Practice

Program, Weill Cornell Medicine, in 2015; the Geisel School of Medicine, Dartmouth College, in 2017; the Department of Chemistry, University of California at Santa Barbara, Santa Barbara, in 2018; the Citigroup Biomedical Imaging Center, Weill Cornell Medicine, in 2018; the National Cancer Institute, National Institutes of Health (NIH), in 2019; and the Department of Radiology, Weill Cornell Medicine, in 2019. His research interests include signal and image processing and magnetic resonance spectroscopy and imaging.

Dr. Srivastava is a member of the International Electron Paramagnetic Resonance Society, the Biophysical Society, the American Chemical Society, the International Society of Magnetic Resonance, and the New York Academy of Sciences. He was a Student Member of the Institution of Electronics and Telecommunications Engineers, from 2007 to 2011. He was a nominated member of the Clinton Global Initiative University, from 2017 to 2019. He was a recipient of the Certificate of Merit from JUET, in 2010; the Ericsson's University Relationship Program (EMPOWER) Fellowship–India, in 2010; the Summer Research Fellowship from the Indian Institute of Science Education and Research–Kolkata, India, in 2010; the Vice-Chancellor's Gold Medal from JUET, in 2011; the Ph.D. Technology Commercialization Fellowship from Cornell University, in 2016; the Graduate School Research Grant from Cornell University, in 2017; the Electron Spin Resonance Technology Transfer Experience Award by SharedEPR, in 2017 and 2018; the Alumni Association Academic Enrichment Grant from Cornell University, in 2017; the Phool Prakash and Rukmini Sahai Graduate Fellowship from Cornell University, in 2017; the Clinton Global Initiative-University Pitch Competition Award, in 2018; and the Cornell Technology Acceleration and Maturation Award from Cornell University, in 2019. He was the finalist of the NIH Director's Early Independence Award, in 2019, and the Bruker ESR Thesis Prize by Royal Society of Chemistry, in 2019. During the Ph.D. studies, he was a recipient of many conference travel grants, such as the Graduate School, Cornell University, in 2016 and 2017; the 58th Rocky Mountain Conference on Magnetic Resonance, in 2016; the Entrepreneurship@Cornell, Cornell University, in 2017; the Office of Engagement Initiatives, Cornell University, in 2017; the International Conference on EPR Spectroscopy and Imaging of Biological Systems, in 2017; and the 20th International Society of Magnetic Resonance Meeting, in 2017.

REFERENCES

[1]. Srivastava M, Anderson CL, and Freed JH, "A new wavelet denoising method for selecting decomposition levels and noise thresholds," IEEE Access, vol. 4, pp. 3862–3877, 2016. [PubMed: 27795877]

[2]. Srivastava M, Dzikovski B, and Freed JH, "Extraction of weak spectroscopic signals with high fidelity: Examples from ESR," J. Phys. Chem. A, vol. 125, no. 20, pp. 4480–4487, May 2021. [PubMed: 34009996]

[3]. Fodor IK, "Denoising through wavelet shrinkage: An empirical study," J. Electron. Imag, vol. 12, no. 1, p. 151, Jan. 2003.

[4]. Wink AM and Roerdink JBJM, "Denoising functional MR images: A comparison of wavelet denoising and Gaussian smoothing," IEEE Trans. Med. Imag, vol. 23, no. 3, pp. 374–387, Mar. 2004.

[5]. Whitcher B, Guttorp P, and Percival DB, "Wavelet analysis of covariance with application to atmospheric time series," J. Geophys. Res., Atmos, vol. 105, no. D11, pp. 14941–14962, Jun. 2000.

[6]. Cazelles B, Chavez M, Berteaux D, Ménard F, Vik JO, Jenouvrier S, and Stenseth NC, "Wavelet analysis of ecological time series," Oecologia, vol. 156, no. 2, pp. 287–304, May 2008. [PubMed: 18322705]

[7]. Xu M, Han M, and Lin H, "Wavelet-denoising multiple echo state networks for multivariate time series prediction," Inf. Sci, vol. 465, pp. 439–458, Oct. 2018.

[8]. Gertz SD et al. , "Isotropic wavelet analysis for identification of coronary atherosclerotic plaque components from computed tomography," Circulation, vol. 114, no. suppl_18, p. II_817, 2006, doi: 10.1161/circ.114.suppl_18.II_817-c.

[9]. Katunin A, Dańczak M, and Kostka P, "Automated identification and classification of internal defects in composite structures using computed tomography and 3D wavelet analysis," Arch. Civil Mech. Eng, vol. 15, no. 2, pp. 436–448, Feb. 2015.

[10]. Mohammadi S and Leventouri T, "A study of wavelet-based denoising and a new shrinkage function for low-dose CT scans," Biomed. Phys. Eng. Exp, vol. 5, no. 3, Mar. 2019, Art. no. 035018.

[11]. Brammer MJ, "Multidimensional wavelet analysis of functional magnetic resonance images," Hum. Brain Mapping, vol. 6, nos. 5–6, pp. 378–382, 1998.

[12]. Delakis I, Hammad O, and Kitney RI, "Wavelet-based de-noising algorithm for images acquired with parallel magnetic resonance imaging (MRI)," Phys. Med. Biol, vol. 52, no. 13, pp. 3741–3751, Jul. 2007. [PubMed: 17664574]

[13]. Islam MS and Islam R, "Multiscale wavelet-based regularized reconstruction algorithm for three-dimensional compressed sensing magnetic resonance imaging," Signal, Image Video Process, vol. 15, no. 7, pp. 1487–1495, Oct. 2021.

[14]. Buranachai C, Kamiyama D, Chiba A, Williams BD, and Clegg RM, "Rapid frequency-domain FLIM spinning disk confocal microscope: Lifetime resolution, image improvement and wavelet analysis," J. Fluorescence, vol. 18, no. 5, pp. 929–942, Sep. 2008.

[15]. Asfour H, Swift LM, Sarvazyan N, Doroslovacki M, and Kay MW, "Signal decomposition of transmembrane voltage-sensitive dye fluorescence using a multiresolution wavelet analysis," IEEE Trans. Biomed. Eng, vol. 58, no. 7, pp. 2083–2093, Jul. 2011. [PubMed: 21511560]

[16]. Hüpfel M, Kobitski AY, Zhang W, and Nienhaus GU, "Wavelet-based background and noise removal for fluorescence microscopy images," Biophys. J, vol. 120, no. 3, p. 359a, Feb. 2021.

[17]. Hu Y, Shen A, Jiang T, Ai Y, and Hu J, "Classification of normal and malignant human gastric mucosa tissue with confocal Raman microspectroscopy and wavelet analysis," Spectrochimica Acta A, Mol. Biomolecular Spectrosc, vol. 69, no. 2, pp. 378–382, Feb. 2008.

[18]. Kumar N, Siddiqi AH, and Alam K, "Raman spectral data de-noising based on wavelet analysis," Int. J. Comput. Appl, vol. 102, no. 16, pp. 15–18, Sep. 2014.

[19]. Sun P, Shi Y, Li L, Wang G, Guan J, Qian F, and Yu Y, "Multi-scale wavelet thresholding denoising algorithm of Raman spectrum," in Proc. Int. Conf. Opt. Instrum. Technol., Optoelectron. Imag./Spectrosc. Signal Process. Technol, Mar. 2020, p. 114380M.

[20]. Wassner H and Chollet G, "New cepstral representation using wavelet analysis and spectral transformation for robust speech recognition," in Proc. 4th Int. Conf. Spoken Lang. Process. (ICSLP), Oct. 1996, pp. 260–263.

[21]. Trivedi N, Kumar V, Singh S, Ahuja S, and Chadha R, "Speech recognition by wavelet analysis," Int. J. Comput. Appl, vol. 15, no. 8, pp. 27–32, 2011.

[22]. Hidayat R and Winursito A, "A modified MFCC for improved wavelet-based denoising on robust speech recognition," Int. J. Intell. Eng. Syst, vol. 14, no. 1, pp. 12–21, Feb. 2021.

[23]. Xie Y, Zhang Y, and Ye Z, "Short-term traffic volume forecasting using Kalman filter with discrete wavelet decomposition," Comput.-Aided Civil Infrastruct. Eng, vol. 22, no. 5, pp. 326–334, Jul. 2007.

[24]. Yu W, Su J, and Zhang W, "Research on short-term traffic flow prediction based on wavelet de-noising preprocessing," in Proc. 9th Int. Conf. Natural Comput. (ICNC), Jul. 2013, pp. 252–256.

[25]. Peng Y and Xiang W, "Short-term traffic volume prediction using GA-BP based on wavelet denoising and phase space reconstruction," Phys. A, Stat. Mech. Appl, vol. 549, Jul. 2020, Art. no. 123913.

[26]. Bryant JH, Electron Paramagnetic Resonance Image Reconstruction for Arbitrary Projection Sampling and Regions of Interest. The University of Chicago, Chicago, IL, USA, 2011.

[27]. Roy AS and Srivastava M, "Hyperfine decoupling of ESR spectra using wavelet transform," Magnetochemistry, vol. 8, no. 3, p. 32, Mar. 2022. [PubMed: 37475982]

[28]. Addison PS, The Illustrated Wavelet Transform Handbook: Introductory Theory and Applications in Science, Engineering, Medicine and Finance. Boca Raton, FL, USA: CRC Press, 2017.

[29]. Donoho DL, "De-noising by soft-thresholding," IEEE Trans. Inf. Theory, vol. 41, no. 3, pp. 613–627, May 1995.

[30]. Donoho DL and Johnstone IM, "Ideal spatial adaptation by wavelet shrinkage," Biometrika, vol. 81, no. 3, p. 425, Aug. 1994.

[31]. Pasti L, Walczak B, Massart DL, and Reschiglian P, "Optimization of signal denoising in discrete wavelet transform," Chemometric Intell. Lab. Syst, vol. 48, no. 1, pp. 21–34, Jun. 1999.

[32]. Li F, Meng G, Kageyama K, Su Z, and Ye L, "Optimal mother wavelet selection for Lamb wave analyses," J. Intell. Mater. Syst. Struct, vol. 20, no. 10, pp. 1147–1161, Jul. 2009.

[33]. Pies S, Landeche A, Leftwich KM, and Ioup J, "Machine learning methods for finding the best wavelet for audio compression," in Proc. Meetings Acoust, Sep. 2023, vol. 51, no. 1, Paper 055002.

[34]. Zhang X, Lu B, and Qiao L, "A wavelet selection scheme in underwater discharge signal analysis," EURASIP J. Adv. Signal Process, vol. 2023, no. 1, p. 106, Oct. 2023.

[35]. Moradi M, "Wavelet transform approach for denoising and decomposition of satellite-derived ocean color time-series: Selection of optimal mother wavelet," Adv. Space Res, vol. 69, no. 7, pp. 2724–2744, Apr. 2022.

[36]. Zamorano M, Gómez Garcia MJ, and Castejón C, "Selection of a mother wavelet as identification pattern for the detection of cracks in shafts," J. Vib. Control, vol. 28, nos. 21–22, pp. 3152–3161, Nov. 2022.

[37]. Gandhi T, Panigrahi BK, and Anand S, "A comparative study of wavelet families for EEG signal classification," Neurocomputing, vol. 74, no. 17, pp. 3051–3057, Oct. 2011.

[38]. Maheswaran R and Khosa R, "Comparative study of different wavelets for hydrologic forecasting," Comput. Geosci, vol. 46, pp. 284–295, Sep. 2012.

[39]. Strömbergsson D, Marklund P, Berglund K, Saari J, and Thomson A, "Mother wavelet selection in the discrete wavelet transform for condition monitoring of wind turbine drivetrain bearings," Wind Energy, vol. 22, no. 11, pp. 1581–1592, Nov. 2019.

[40]. Bekerman W and Srivastava M, "Determining decomposition levels for wavelet denoising using sparsity plot," IEEE Access, vol. 9, pp. 110582–110591, 2021.

[41]. Weil JA and Bolton JR, Electron Paramagnetic Resonance: Elementary Theory and Practical Applications. Hoboken, NJ, USA: Wiley, 2007.

[42]. Freed JH, "New technologies in electron spin resonance," Annu. Rev. Phys. Chem, vol. 51, no. 1, pp. 655–689, 2000. [PubMed: 11031296]

[43]. Freed JH, "ESR and molecular dynamics," in Biomedical EPR, Part B: Methodology, Instrumentation, and Dynamics, Eaton SR, Eaton GR, and Berliner LJ, Eds. Boston, MA, USA: Springer, 2005, pp. 239–268, doi: 10.1007/0-306-48533-8_9.

[44]. Hofbauer W, Earle KA, Dunnam CR, Moscicki JK, and Freed JH, "High-power 95 GHz pulsed electron spin resonance spectrometer," Rev. Sci. Instrum, vol. 75, no. 5, pp. 1194–1208, May 2004.

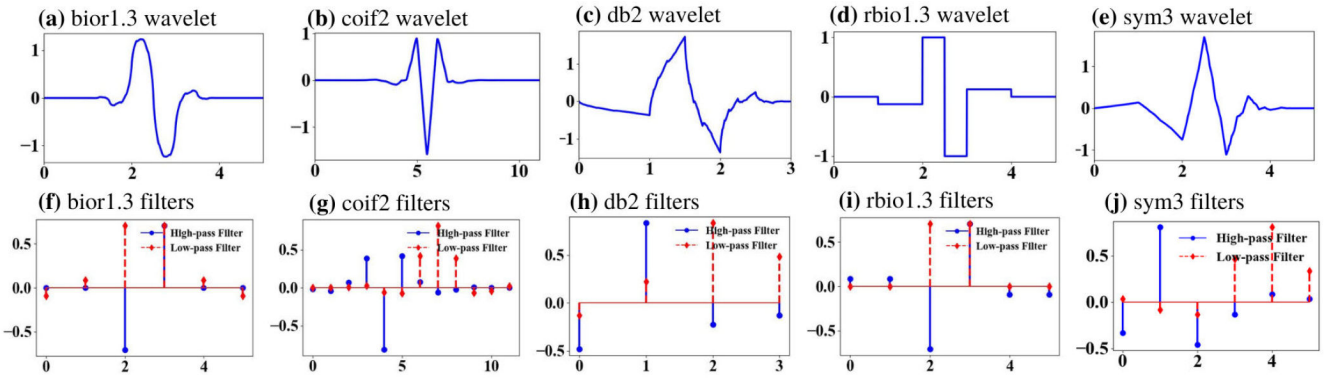

FIGURE 1.

Plot of the wavelet function and corresponding High-pass and Low-pass filters of (a, f) bior1.3, (b, g) coif2, (c, h) db2, (d, i) rbio1.3 and (e, j) sym3 wavelets.

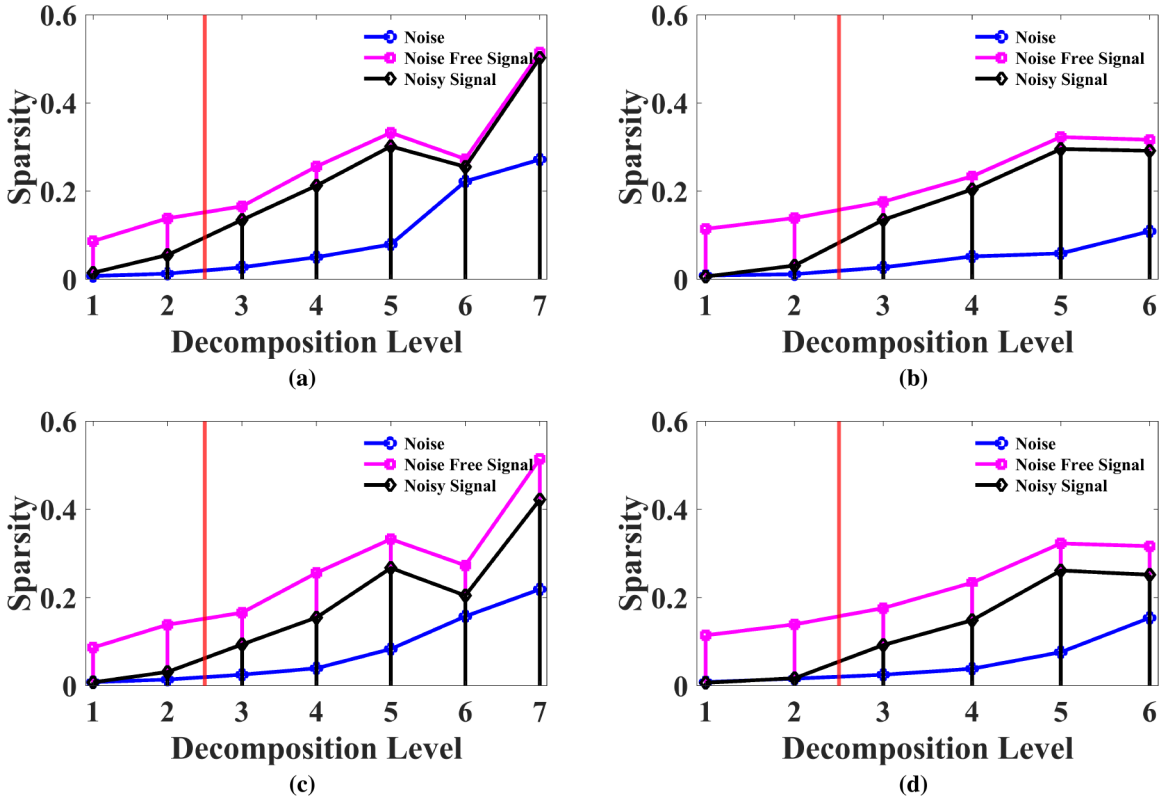

FIGURE 2.

The sparsity plot of wavelets (*a*, *c*) *sym2*, (b, d) *coif 2* for white Gaussian noise, noise-free signal and noisy signal of (a, b) SNR 30 and (c, d) SNR 10. The vertical line denote the optimal decomposition level that separates noisy and noise-free Detail coefficients.

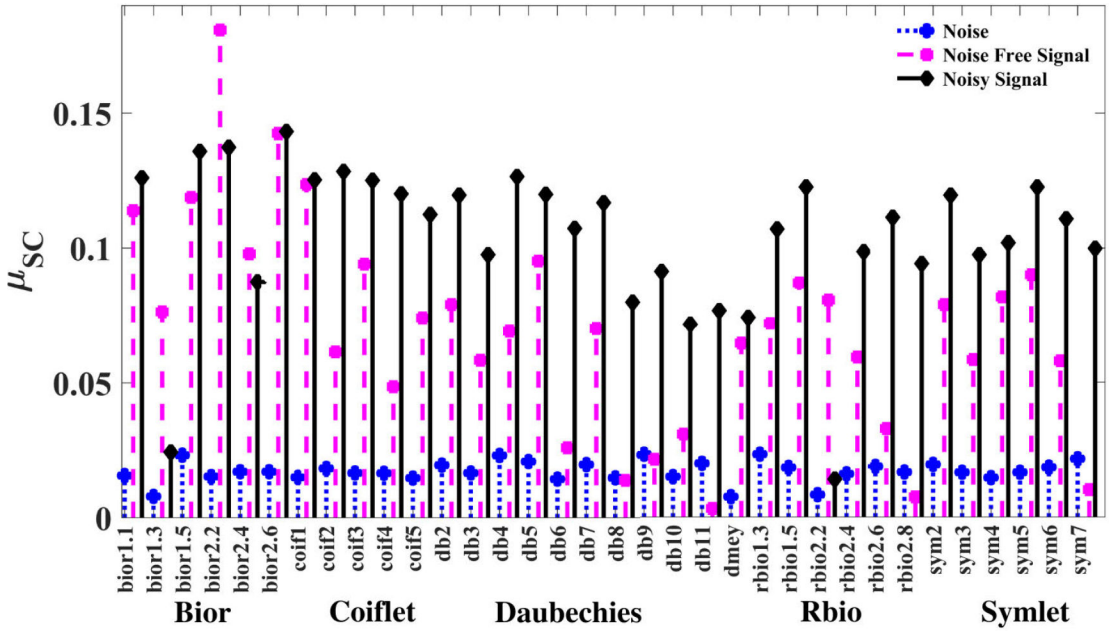

FIGURE 3.

Stem plot of the mean of sparsity change of white Gaussian noise, noise-free and noisy simulated signals of SNR-30.

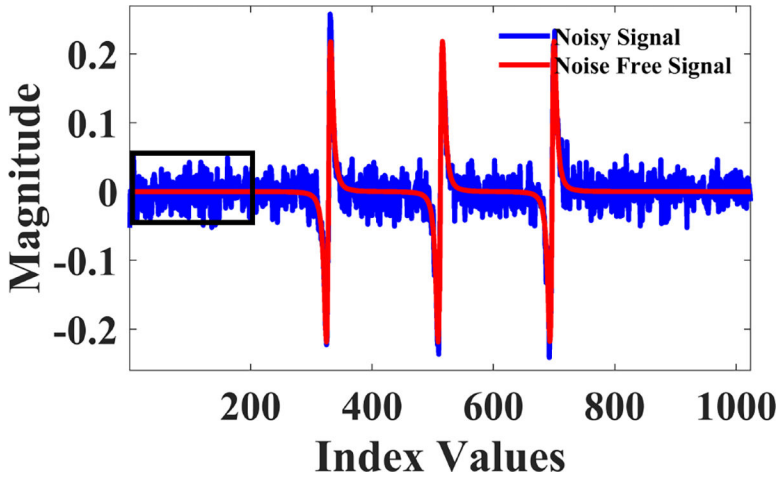

FIGURE 4.

Plot of the simulated noise-free and noisy signal of SNR-10. The region inside rectangle is used for calculation of $Noise_{rms}$.

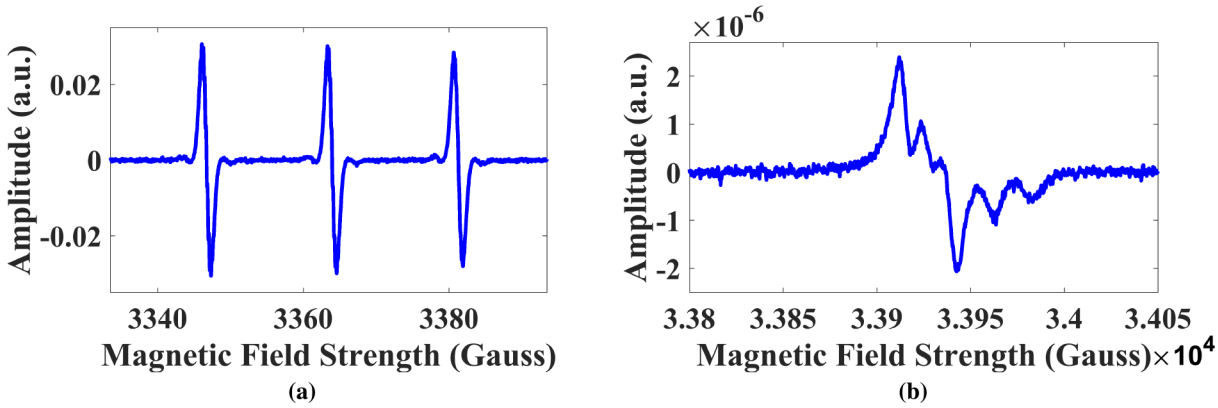

FIGURE 5.

ESR signals obtained from (a) a Bruker X Band (9.4 GHz) spectrometer averaged at 500 scans and (b) in-house built (ACERT) W Band (95 GHz) spectrometer averaged at 18 scans.

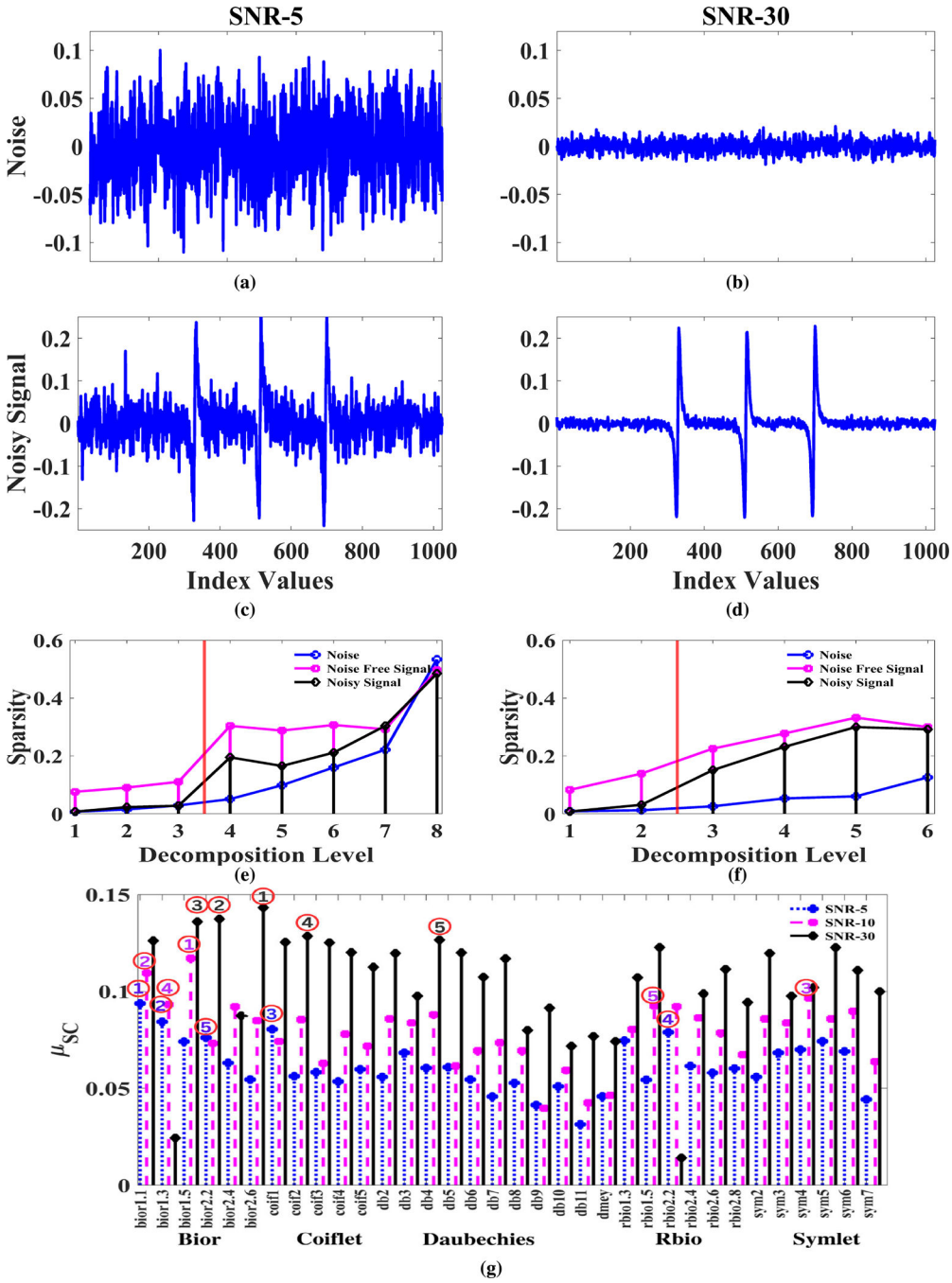

FIGURE 6.

Generated Gaussian noise to achieve (a) SNR-5 and (b) SNR-30. Signal of (c) SNR-5 and (d) SNR-30 after addition of noise. The sparsity plot of noise, noise-free signal and noisy signal of (e) SNR-5 and bior1.1 and (f) SNR-30 and bior2.6 wavelets. Red vertical line in the sparsity plot indicates the separation between noisy and noise-free Detail components. (g) Stem plot of the μ_{sc} of the simulated data for SNR-5, 10 and 30. Top five selected wavelets are highlighted corresponding to their number inside circles.

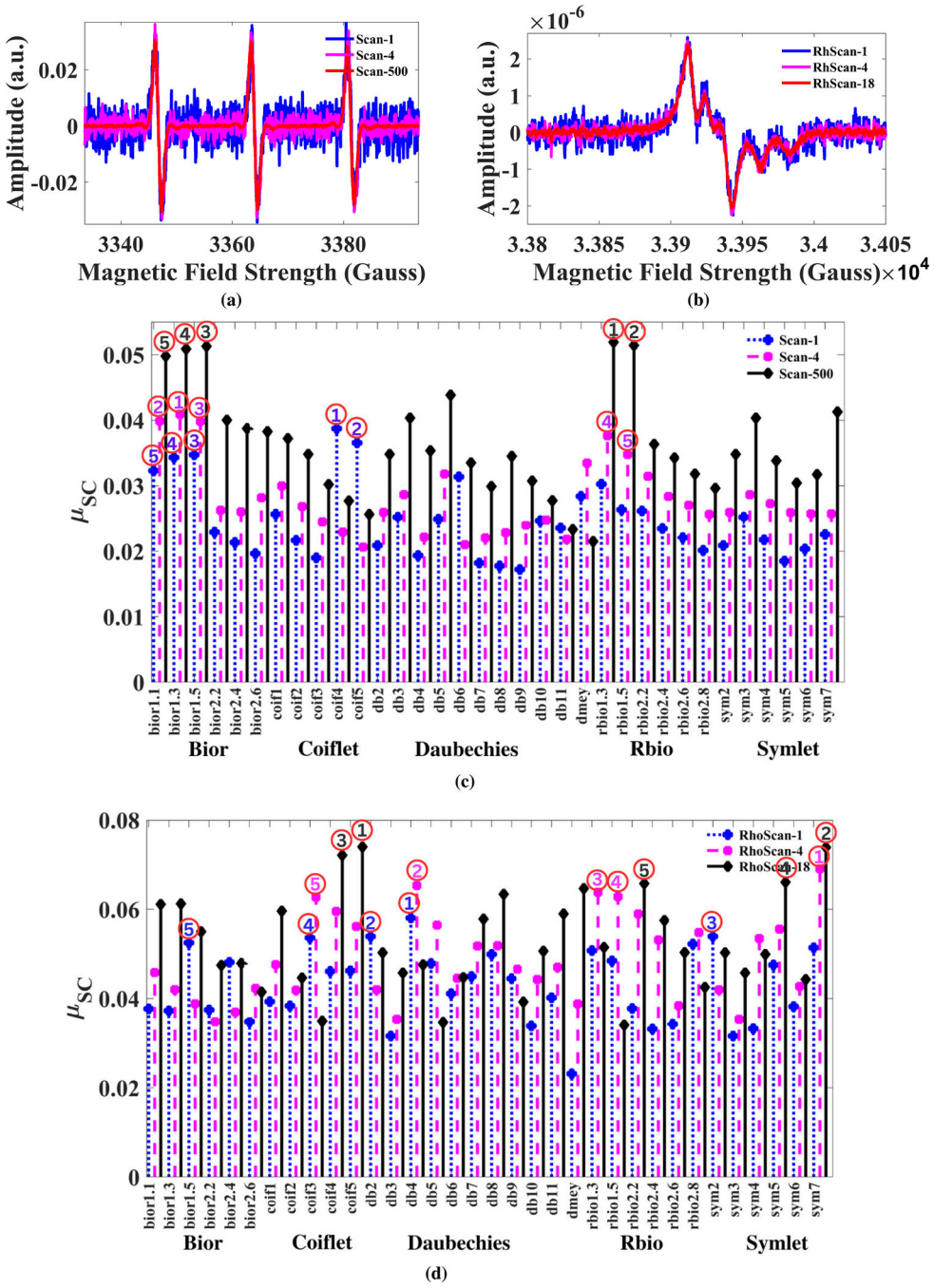

FIGURE 7.

Signals averaged at various scans collected from (a) the commercial spectrometer, (b) in-house built spectrometer. Stem plot of the μ_{sc} of all scans for signals recorded from (c) the commercial spectrometer and (d) in-house built spectrometer. Top five selected wavelets are highlighted corresponding to their number inside circles.

TABLE 1.

Description of symbols used.

Symbol	Description
X	Input signal.
L_{D_j}	Length of Detail component at *jth* decomposition level.
L_f	Length of wavelet filter.
R_j	Ratio of length of Detail component to the length of wavelet filter.
D_j	Detail component at decomposition level *j*.
$D_j[k]$	Detail component at index k for decomposition level *j*.
S_j	Sparsity at level *j*.
q_j	Length of the Detail component at decomposition level *j*.
N	Maximum possible decomposition level.
ΔS	Sparsity change between adjacent levels.
ΔS_j	Sparsity change at *jth* level.
κ	Optimal decomposition level that separates noisy and noise-free Detail coefficients.
μ_{SC}	Mean of sparsity change.
std	Standard deviation.
$Noise_{rms}$	Root mean square of noise.
$Signal_{peak}$	Maximum value of the signal.
SNR	Signal to noise ratio.

TABLE 2.

Wavelet sample space used for the optimal wavelet selection.

Biorthogonal	Coiflet	Daubechies	Reverse biorthogonal	Symlet
bior1.1	coif1	db2	rbio1.3	sym2
bior1.3	coif2	db3	rbio1.5	sym3
bior1.5	coif3	db4	rbio2.2	sym4
bior2.2	coif4	db5	rbio2.4	sym5
bior2.4	coif5	db6	rbio2.6	sym6
bior2.6		db7	rbio2.8	sym7
		db8		
		db9		
		db10		
		db11		

TABLE 3.

Length of the detail coefficients, filter length, and ratio of L_{D_j}/L_f of Coiflet wavelet family are shown in the table. L_{D_j} : length of detail component at *jth* decomposition level; L_f : filter length; R_j : ratio of L_{D_j}/L_f.

Levels	coifl			Coif2			coif3			coif4			coif5		
	L_{D_j}	L_f	R_j	L_{D_j}	L_f	R_j	L_{D_j}	L_f	R_j	L_{D_j}	L_f	R_j	L_{D_j}	L_f	R_j
1	514	6	85.7	517	12	43.1	520	18	28.9	523	24	21.8	526	30	17.5
2	259	6	43.2	264	12	22.0	268	18	14.9	273	24	11.4	277	30	9.2
3	132	6	22.0	137	12	11.4	142	18	7.9	148	24	6.2	153	30	5.1
4	68	6	11.3	74	12	6.2	79	18	4.4	85	24	3.5	91	30	3.0
5	36	6	6.0	42	12	3.5	48	18	2.7	54	24	2.3	60	30	2.0
6	20	6	3.3	26	12	2.2	32	18	1.8	38	24	1.6	44	30	1.4
7	12	6	2.0	18	12	1.5	24	18	1.3	30	24	1.2	36	30	1.2
8	8	6	1.3	14	12	1.2	20	18	1.1	26	24	1.1	32	30	1.0
9	6	6	1.0	12	12	1.0	18	18	1.0	24	24	1.0	30	30	1.0
10	5	6	0.8	11	12	0.9	17	18	0.9	23	24	0.9	29	30	0.9

TABLE 4.

Details of the wavelet families and their wavelet numbers, filter length, effective decomposition level, and L_{D_j}/L_f are presented in this table. EDL: effective decomposition level; L_f : filter length; R_j : ratio of L_{D_j}/L_f.

Daubechies				Coiflet				Symlet				Biorthogonal				Reverse biorthogonal			
Wavelet	L_f	**EDL**	R_j	**Wavelet**	L_f	**EDL**	R_j	**Wavelet**	L_f	**EDL**	R_j	**Wavelet**	L_f	**EDL**	R_j	**Wavelet**	L_f	**EDL**	R_j
db2	4	7	2.5	coif1	6	7	2.0	sym2	4	7	2.5	bior1.1	2	8	2.0	rbio1.3	6	7	2.0
db3	6	7	2.0	coif2	12	6	2.2	sym3	6	7	2.0	bior1.3	6	7	2.0	rbio1.5	10	7	1.6
db4	8	7	1.8	coif3	18	6	1.8	sym4	8	7	1.8	bior1.5	10	7	1.6	rbio2.2	6	7	2.0
db5	10	7	1.6	coif4	24	6	1.6	sym5	10	7	1.6	bior2.2	6	7	2.0	rbio2.4	10	7	1.6
db6	12	6	2.2	coif5	30	5	2.0	sym6	12	6	2.2	bior2.4	10	7	1.6	rbio2.6	14	6	2.0
db7	14	6	2.0					sym7	14	6	2.0	bior2.6	14	6	2.0	rbio2.8	18	6	1.8
db8	16	6	1.9																
db9	18	6	1.8																
db10	20	6	1.7																
db11	22	6	1.6																

TABLE 5.

Table represents the first five wavelets corresponding to the highest μ_{sc}, their optimal decomposition level and the μ_{sc} values for simulated signals of various SNRs.

SNR-5			SNR-10			SNR-30			SNR-50		
Wavelet	κ	μ_{sc}	**Wavelet**	κ	μ_{sc}	**Wavelet**	κ	μ_{sc}	**Wavelet**	κ	μ_{sc}
bior1.1	3	0.0938	bior1.5	2	0.1171	bior2.6	2	0.1433	bior2.2	2	0.1673
bior1.3	3	0.0843	bior1.1	3	0.1095	bior2.2	2	0.1374	bior2.6	2	0.1584
coif1	3	0.0805	sym4	3	0.0966	bior1.5	2	0.1359	coif3	2	0.1520
rbio2.2	3	0.0789	biorl.3	3	0.0932	coif2	2	0.1285	bior1.5	2	0.1451
bior2.2	3	0.0761	rbio1.5	2	0.0925	db4	2	0.1266	db5	2	0.1439

TABLE 6.

Table represent the first five wavelets corresponding to the highest μ_{sc}, their optimal decomposition level and the μ_{sc} of experimental signals averaged at different scans collected using the commercial spectrometer.

Scan-1			Scan-4			Scan-500		
Wavelet	κ	μ_{sc}	**Wavelet**	κ	μ_{sc}	**Wavelet**	κ	μ_{sc}
coif4	6	0.0387	bior1.3	5	0.0409	rbio1.3	5	0.0519
coif5	6	0.0366	bior1.1	5	0.0399	rbio1.5	5	0.0514
bior1.5	5	0.0347	bior1.5	5	0.0398	bior1.5	5	0.0513
bior1.3	5	0.0343	rbio1.3	5	0.0377	bior1.3	5	0.0509
bior1.1	5	0.0323	rbio1.5	5	0.0348	bior1.1	5	0.0498

TABLE 7.

Table represents the first five wavelets corresponding to the highest μ_{sc}, their optimal decomposition level and the μ_{sc} of experimental signals averaged at different scans collected using the in-house built spectrometer.

RhoScan-1			RhoScan-4			RhoScan-18		
Wavelet	κ	μ_{sc}	**Wavelet**	κ	μ_{sc}	**Wavelet**	κ	μ_{sc}
db4	4	0.0580	sym7	4	0.0690	coif5	4	0.0740
db2	4	0.0539	db4	4	0.0653	sym7	4	0.0739
sym2	4	0.0539	rbio1.3	4	0.0638	coif4	4	0.0721
coif3	4	0.0536	rbio1.5	4	0.0628	sym5	4	0.0661
bior1.5	4	0.0525	coif3	4	0.0627	rbio2.2	3	0.0658